

New optical method for measuring small-angle rotations

Pan Shi and Erik Stijns

To measure small-angle rotations, the two mirrors of a Michelson interferometer are replaced by right-angle prisms. Rotation of the latter shifts the interference pattern. Measurement of that shift gives, after calibration, the rotation. The experimental setup is insensitive to vibrations, provides good linearity between $+5^\circ$ and -5° , and has a resolution of 10^{-4} deg.

I. Introduction

Although the measurement of rotations is a mechanical problem, optical methods are often used, e.g., in optical shaft encoders or moiré pattern techniques. The sensitivity can be increased by orders of magnitude with interferometric techniques, which require a coherent light source. Some of those setups are so extremely sensitive that they have only a limited range of use: in 1974 Chapman¹ obtained an instrumental resolution of 57 msec of arc/fringe. Others make use of special lasers, which render such setups rather expensive.²

We present here another method, which uses only off-the-shelf lasers and optics, and which gives nevertheless satisfactory results as concerns sensitivity, ease of use, and insensitivity to parasitic vibrations.

II. Basic Setup

The basic idea consists of using a Michelson interferometer, in which one of the two mirrors is replaced by a device with the following two properties: (a) it reflects the light beam back on itself and (b) it can rotate around an axis perpendicular to the plane of the figure. When rotating, the optical path length in the device is a linear function of the angle of rotation.

Because of property (a) an interference pattern is formed at the screen; property (b) implies that the interference pattern shifts during the rotation of the device. By measuring that shift one can, after calibration, calculate the rotation.

III. Right-Angle Prism as a Retroreflector

This device is made by using a right-angle prism as shown in Fig. 1. The laser ray is sent via a beam splitter to that prism. The ray leaving the prism is parallel to the incoming ray and is then reflected on a fixed perpendicular mirror $M2$. Consequently, that ray follows exactly the same path back to the interferometer. This is also true when the prism is rotated, but then the optical path length changes, and the interference pattern shifts. The shift is measured by detector D , which counts the number of fringes passing it.

The rest of this section is devoted to an analysis of the change of the optical path length as a function of the angle of rotation. To calculate it, consider Fig. 2. The light beam enters the prism at point Do ; the (vertical) axis of rotation is also situated at that same point. The optical path, measured from Do to mirror $M2$ is then

$$P = [n(DoE + EF + FG) + GM], \quad (1)$$

where n is the refractive index of the prism. Path P depends on the angle of rotation; by geometrical arguments one can show that, after rotating over an angle θ , the path is given by

$$P(\theta) = \frac{\sqrt{2}an}{\cos\alpha} + GM, \quad (2)$$

with

$$n \sin\alpha = \sin\theta, \quad (3)$$

$$GM = GoMo + \sin\theta(\sqrt{2}a + \sqrt{2}a \tan\alpha - 2\delta). \quad (4)$$

Distances a and δ are shown in the figure.

Taking $\theta = 0$ as the starting position, it follows that the change in optical path after a rotation θ is

$$\begin{aligned} \Delta P &= P(\theta) - P(0) \\ &= \sqrt{2}an(\cos\alpha - 1) + (\sqrt{2}a - 2\delta) \sin\theta. \end{aligned} \quad (5)$$

This formula is valid for both positive and negative values of θ .

The authors are with Free University of Brussels, Applied Physics Department, Pleinlaan 2, B-1050 Brussels, Belgium.

Received 30 October 1987.

0003-6935/88/204342-03\$02.00/0.

© 1988 Optical Society of America.

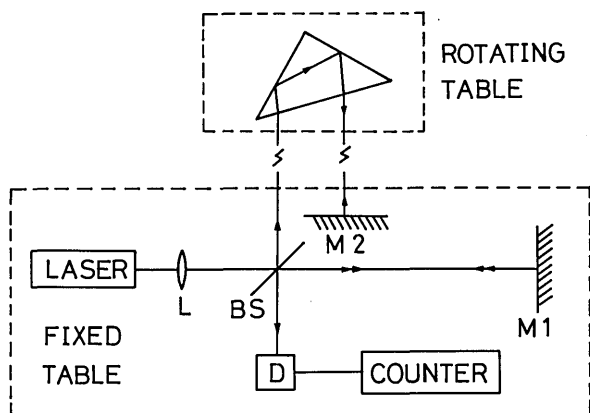


Fig. 1. Experimental setup with a single prism.

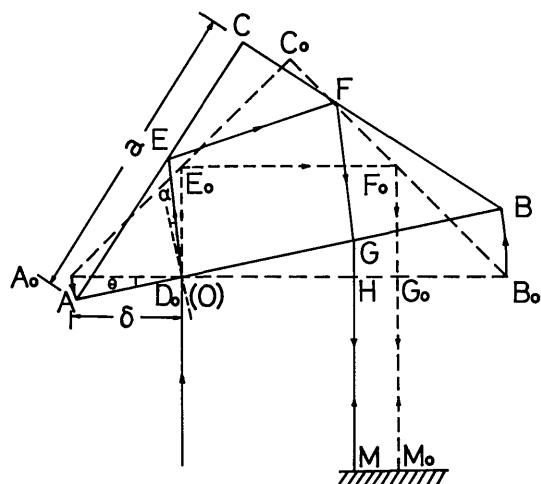


Fig. 2. Path of the light ray before and after rotation of the prism; the light ray enters the prism at the axis of rotation.

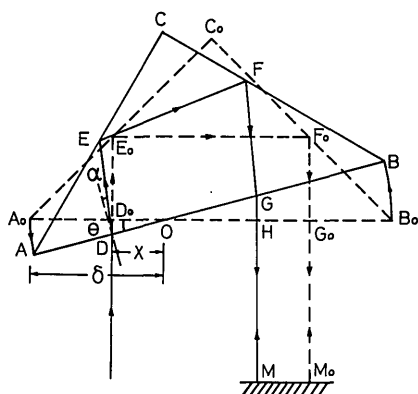


Fig. 3. Path of the light ray before and after rotation of the prism; the axis of rotation is displaced in the x direction.

Consider next what happens when the axis of rotation is displaced, and consider first the simple case of a displacement along the hypotenuse of the triangle, as shown in Fig. 3. It can easily be shown that Eq. (5) is still valid.

If the position of the axis of rotation is completely arbitrary (Fig. 4), the optical path length is

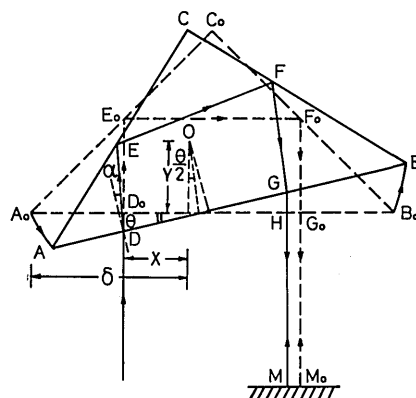


Fig. 4. Path of the light ray before and after rotation of the prism; the axis of rotation is displaced in the x and y directions.

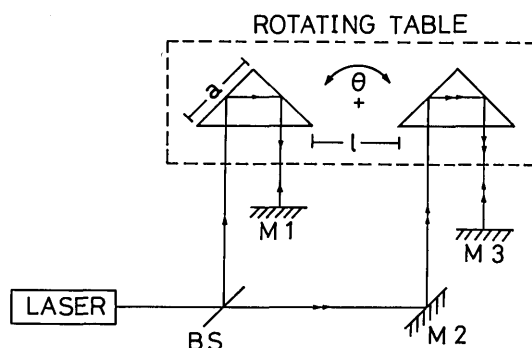


Fig. 5. Basic setup with two prisms.

$$\Delta P = \sqrt{2}an(\cos\alpha - 1) + \left(\sqrt{2}a - 2\delta + 2y \tan \frac{\theta}{2}\right) \sin\theta. \quad (6)$$

For small rotations this reduces to

$$\Delta P \approx (\sqrt{2}a - 2\delta)\theta + \left(y - \frac{a}{\sqrt{2}n}\right)\theta^2. \quad (7)$$

This formula shows that it is possible to improve the linearity by choosing

$$y = \frac{a}{\sqrt{2}n}. \quad (8)$$

Only third-order deviations from linearity remain, and they are negligible for small rotations.

IV. Balanced Setup

An improvement of the previous setup was suggested by Chapman³ and is shown in Fig. 5. The light beam of the second arm is also sent to the rotating table, where it is reflected by a second right-angle prism. Because of the symmetry, both the linearity and the sensitivity are greatly increased. If we take two equal prisms, with sides a and distance between them equal to l , the change of the optical path length can be shown to be

$$\Delta P = 2(\sqrt{2}a + l) \sin\theta. \quad (9)$$

It turns out that the actual position of the axis of rotation has no importance: one always finds the same formula. Because Eq. (9) depends only on the

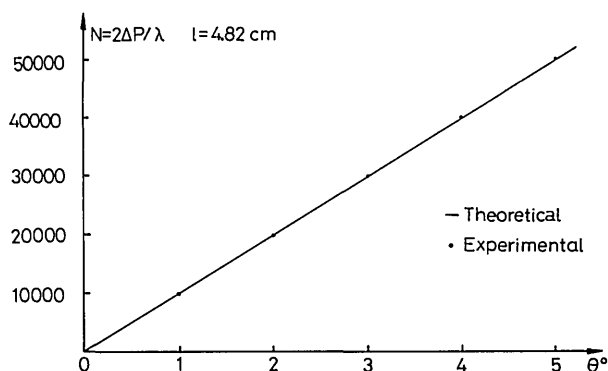


Fig. 6. Experimental points compared to the theoretical curve.

sine of the angle and not, as Eq. (6) does, on other trigonometric functions, the linearity of Eq. (9) for small angles is better than the linearity of Eq. (6). Moreover this symmetrical setup can increase the sensitivity by more than an order of magnitude: it suffices therefore to take l large enough.

V. Experimental Verification

The setup of Fig. 5 was made and Eq. (9) was checked. Two identical right-angle prisms, with sides $a = 30$ mm, were fixed on a base. The distance between them was adjusted to $l = 48.2$ mm to obtain a shift of the interference pattern of 10,000 fringes for a rotation of 1° . A He-Ne laser, with a small diverging lens, was used as the light source. The shift of the interference pattern was measured with two photodiodes, positioned very close together.³ Both signals were sent, after amplification, to a logic controller. Both photodiodes see the same number of fringes, but with a small phase shift between them. The sign of the phase shift depends on the direction of movement of the fringe pattern and consequently on the direction of rotation. The electronic circuit transforms each fringe to an electronic pulse. The logic controller now assigns each of the pulses a plus or minus sign, depending on the direction of movement. Those pulses, to-

gether with their signs, are sent to an up-down counter, which counts the algebraic sum. This setup reduces the spurious pulses generated by vibrations; indeed, vibrations around equilibrium give as many plus pulses as minus pulses, and consequently no net result is measured at the counter. So only real rotations are measured and vibrations are neglected.

The experimental results are shown in Fig. 6. Each experimental point is the average of twenty measurements; the relative standard deviation σ/N ranges between 0.05% and 0.2%.

VI. Limits

Although from a theoretical point of view the total angle of rotation can be large, we could only measure rotations in the range from $+5^\circ$ to -5° , because, at larger angles, the light fluxes at the detectors were too small to be measured. The distance between the fixed part of the interferometer and the rotating table could be large: we could measure up to a distance of 5 m. Vibration cause no real problem in the measurements.

VII. Conclusions

Measuring small-angle rotations with a setup with two right-angle prisms is a simple and accurate method. It has good linearity; the sensitivity goes down to 10^{-4} degree $\approx 2 \times 10^{-3}$ mrad/fringe, and it is insensitive to vibrations.

We would like to acknowledge S. Cools who worked out the first experimental setup and especially G. D. Chapman whose remarks turned the original idea into a practical device. A preliminary version of this work was presented at the SPIE Quebec Conference.⁴

Pan Shi is on leave from the Dalian Institute of Technology.

References

1. G. D. Chapman, "Interferometric Angular Measurement," *Appl. Opt.* **13**, 1646 (1974).
2. Hewlett-Packard laser measurement system 5526A.
3. G. D. Chapman, National Research Council of Canada; private communications.
4. E. Stijns, "Measuring Small Rotation Rates with a Modified Michelson Interferometer," *Proc. Soc. Photo-Opt. Instrum. Eng.* **661**, 264 (1986).

NASA continued from page 4330

Improved charge-coupled imager for x rays

A virtual-phase charge-coupled device has been proposed to improve the imaging of x rays with photon energies of 0.2–10 keV. The anticipated benefits of the new design include higher spatial and spectral resolution and greater quantum efficiency at low photon energies. Potential uses include imaging spectrometers for x-ray astronomy, investigations of plasmas, and x-ray crystallography.

In a conventional multiphase charge-coupled device, the sensitivity to photons of less than about 2 keV is degraded by the absorption of these photons in such dead layers as the oxide and gate structures. Sensitivity can be restored by the use of a virtual-phase configuration and by decreasing the thickness of the oxide in the virtual phase to 500 Å. However, without further modification, a conventional virtual-phase charge-coupled device exhibits a loss of spatial resolution with photons of 2 to 10 keV. Such photons are absorbed below the charge-carrying and depleted regions. When charge is thus gen-

erated below the depleted region, it moves toward the charge-carrying region and spreads out. Thus, portions of the charge are detected in several adjacent picture elements whereas it is desired to detect it only in the picture element or elements struck by the photons.

In the proposed device (see Fig. 8), the depletion depth would be about 10 μm comparable to the thickness (10–15 μm) of the epitaxial layer on which the device is fabricated. This feature is expected to prevent the spreading of photogenerated charge to adjacent picture elements. Thus the device would offer the increased quantum efficiency of the virtual-phase configuration, but without the loss of resolution. The quantum efficiency of the device is predicted to have representative values of 33% at 0.2 keV, 76% at 0.7 keV, 69% at 1.5 keV, 90% at 2.0 keV, 45% at 5.0 keV, and 10% at 10 keV. Numerical simulations indicate that the required deep depletion can be achieved by the use of a high-resistivity substrate doped at $1.5 \times 10^{14} \text{ cm}^{-3}$, with a phosphorus implant of $1.5 \times 10^{12} \text{ cm}^{-2}$ at 190 keV and an arsenic implant of $3 \times 10^{12} \text{ cm}^{-2}$ at 25 keV.

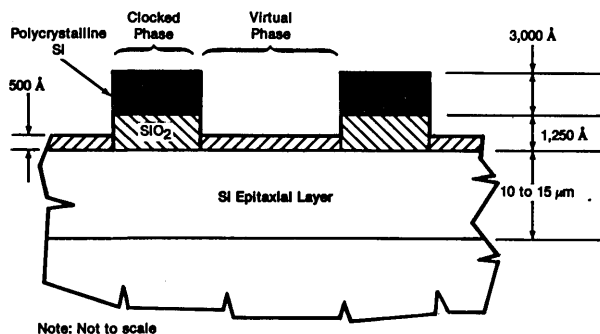


Fig. 8. Improved virtual-phase charge-coupled device would feature a thin layer of oxide in the virtual phase to increase the quantum efficiency and a depletion layer nearly as thick as the epitaxial silicon layer to increase the resolution.

This work was done by Mark Wadsworth of Texas Instruments, Inc., for NASA's Jet Propulsion Laboratory. Inquiries concerning rights for the commercial use of this invention should be addressed to the Patent Counsel. NASA Resident Office-JPL attn: P. F. McCaul, Mail Code 180-801, 4800 Oak Grove Drive, Pasadena, CA 91109. Refer to NPO-17312.

Subroutines for image processing

The Image Processing Library computer program, IPLIB, is a collection of subroutines that facilitate the use of a COMTAL image-processing system driven by an HP 1000 computer. IPLIB uses an HP driver to direct all communications between the HP and a COMTAL Vision One/20 system. Dozens of functions are supplied, along with a test program for each function. Each IPLIB function takes the form of a FORTRAN subroutine invocation with appropriate parameters. The functions include the addition or subtraction of two images with or without scaling, display of color or monochrome images, digitization of the image from a television camera, display of a test pattern, manipulation of bits, and clearing of the screen. IPLIB also provides the capability to read or write points, lines, and pixels from an image; read or write at the location of a cursor; and read or write an array of integers into COMTAL memory. The documentation catalogs the subroutines alphabetically and hierarchically for use as a cross-reference guide.

IPLIB is written in FORTRAN 77 for interactive execution and has been implemented on an HP 1000 computer operating under RTE VI with a central-memory requirement of approximately 64K. IPLIB is intended for use by those familiar with the COMTAL Vision One/20 image-processing system. The program was developed in 1985.

This program was written by Nettie D. Faulcon and James H. Monteith of Langley Research Center and Keith W. Miller of the College of William and Mary. Refer to LAR-13620.

Integrated arrays of IR detectors

A report presents an overview of the technology of integrated arrays of infrared detectors. The report covers arrays now available and those under development. It gives examples of astronomical images that illustrate the potential of infrared arrays for scientific investigations.

Integrated arrays combine detection and readout-multiplexing functions in integral packages. In principle, they can be made from a variety of intrinsic and extrinsic infrared-sensitive materials. Intrinsic materials such as indium antimonide and mercury cadmium telluride are generally employed in photovoltaic detectors. Extrinsic materials such as silicon doped with gallium and silicon doped with arsenic are generally employed in photoconductors or photocapacitors. Techniques for growing crystals, ensuring purity, and

forming contacts are highly advanced, and integrated arrays now achieve nearly ideal performance. Limitations to sensitivity are imposed primarily by the readout circuitry, which can be based on charge-coupled devices, charge-injection devices, or switched field-effect transistors. At present, integrated infrared arrays are made by hybrid methods. Two distinct substrates are used; by designing and processing the detector and multiplexer substrates separately and bump bonding them together, optimum performance can be obtained from each. Indium-bump-bonding techniques are now well established, and interconnection yields of 100% for 32-by-32 arrays are common.

The performances of switched field-effect transistor multiplexers, which offer the greatest sensitivity, are expected to improve further. Meanwhile, development continues on advanced detector and readout concepts like impurity-band conduction arrays, which offer the potential of superior sensitivity, linearity, and ability to withstand radiation. Also promising is an arsenic-doped silicon solid-state photomultiplier; such a device has already counted single-photon events at a wavelength of 28 μm.

This work was done by J. H. Goebel and C. R. McCreight of Ames Research Center. Further information may be found in NASA TM-88357 [N87-18475/NSP], "Integrated Infrared Array Technology." Copies may be purchased [prepayment required] from the National Technical Information Service, Springfield, VA 22161, Telephone (703) 487-4560. Inquiries concerning rights for the commercial use of this invention should be addressed to the Patent Counsel, Ames Research Center attn: D. G. Brekke, Mail Code 200-11, Moffett Field, CA 94035. Refer to ARC-11787.

Short-cycle adsorption refrigerator

A modular adsorption/Joule-Thomson-effect refrigerator offers fast regeneration; when fully developed, its adsorption/desorption cycle time is expected to be only 1 min, as compared with 15 min in previous versions. The refrigerator is smaller and lighter than the previous units of equivalent capacity. A modular configuration makes it relatively easy to build refrigerators that have capacities from milliwatts to watts, according to cooling needs. The refrigerator is intended for the long-term cooling (up to 10 years) of infrared sensors and other equipment in space to temperatures ranging from 4 to 80 K. The only moving parts are small check valves. The refrigerator is designed to be powered mostly by waste heat. A prototype containing twelve compressor modules connected in banks of four provides one-quarter watt of cooling at 25 K. Operating under the control of a computer, the four banks of compressor modules are operated in a phased heating/cooling sequence so that nearly steady cooling is provided for the external heat load.

In the refrigerator, pressurized hydrogen generated by a bank of compressor modules during its heating phase passes through a system of check valves and expands in a Joule-Thomson junction as it enters a refrigeration chamber. There, the hydrogen absorbs heat from the load before it is sucked out by another bank of compressor modules in its cooling phase. In each compressor module, adsorbing charcoal is contained in an inner pressure vessel of stainless steel (see Fig. 9). An open-foam copper matrix holds the charcoal and en-

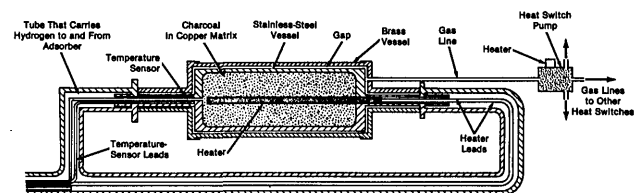


Fig. 9. Heat switch is a gap between concentric cylindrical vessels. For rapid heating and cooling of the core, the gap must be less than about 50 μm.

hances the transfer of heat. A brass outer vessel surrounds the stainless-steel cylinder, and the gap between inner and outer vessels constitutes the heat switch. When the gap is filled with hydrogen, the heat switch exhibits high heat conductance (is on). When the gap is empty, the switch exhibits low heat conductance (is off). A miniature charcoal adsorption pump supplies the gas for the switches in each bank of four compressor modules.

To demonstrate the refrigerator, an electric heater was used to supply heat to each module to cause the desorption of hydrogen from the charcoal in its core. (In a practical model, the heat for desorption would come from waste heat such as that from electronic equipment.) With the heat switch turned off, the adsorber was heated. The adsorber gave off hydrogen as it heated up. When the pressure reached ~ 8.1 MPa, the heater was turned off, and the heat switch was turned on. The adsorber transferred its heat to a liquid-nitrogen bath surrounding the module, readsorbing hydrogen as it cooled and eventually becoming saturated with the gas, ready for another heating cycle. Cooling from 165 K to 85 K took only 50 seconds.

This work was done by C. K. Chan of Caltech for NASA's Jet Propulsion Laboratory. Refer to NPO-16571.

Process makes high grade silicon

A process produces metallurgical-grade silicon from quartz sand. In contrast with some conventional processes, the process does not involve odorous or toxic substances and proceeds at a lower temperature. Like conventional processes, the new process is based on the reaction of silicon dioxide with aluminum, which yields silicon and aluminum oxide: $3\text{SiO}_2 + 4\text{Al} \rightarrow 3\text{Si} + 2\text{Al}_2\text{O}_3$. However, the aluminum for the new process is taken from an operating aluminum-electrolysis cell, and the Al_2O_3 product is returned to the same cell. The aluminum is thus continually recycled and purified, and the purity of the silicon is therefore high as well.

One of the starting materials for the process is 99.5% pure silica sand from natural deposits. (Sand of lower purity can be used but must first be beneficiated.) The sand is introduced into a holding furnace that contains aluminum and electrolyte (molten cryolite) from the electrolysis cell (see Fig. 10), and the resulting mixture is heated to a temperature of 1000–1050°C. A molten aluminum/silicon alloy accumulates in the furnace. The alloy is transferred to a precipitator, and the electrolyte, now rich in Al_2O_3 , is returned to the electrolysis cell. In the precipitator, the alloy is cooled to 700°C, causing globules rich in silicon to solidify, leaving a melt rich in aluminum. The mixture is transferred to a separator, where the solid silicon is extracted and passed to a purifier. The molten aluminum, containing about 12.6% silicon—close to the eutectic composition—is returned to the electrolysis cell.

In the purifier, the solid silicon is treated with molten cryolite that

contains SiO_2 . The residual aluminum in the solid silicon reacts with the SiO_2 to form additional solid silicon. The Al_2O_3 thus produced dissolves in the electrolyte and is returned with it to the electrolysis cell. The electrolyte also contains some silicon, but the material is not wasted because it is recycled. The solid silicon can be recovered directly by remelting at 1410°C or purified further by a salt that is more readily removable than cryolite, by leaching or by a vacuum treatment.

This work was done by Rudolf Keller of EMEC Consultants for Johnson Space Center. In accordance with Public Law 96-517, the contractor has elected to retain title to this invention. Inquiries concerning rights for its commercial use should be addressed to EMEC Consultants, R.D. 3 Roundtop Road, Export, PA 15632. Refer to MSC-21323.

Rotary reactor makes large latex particles

A chemical reactor produces large latex particles up to 100 μm in diameter. Previously such large particles could be produced only in the gravity-free environment of space. On Earth, buoyancy and sedimentation prevented the polymerization reaction from continuing after the particles grew larger than about 3 μm . Stirring to prevent separation did not help; it had to be done so rapidly that it caused violent collisions and consequent flocculation of the soft, sticky particles.

The new reactor includes a cylinder that rotates in a constant-temperature water bath (see Fig. 11). The slow rotation of the cylinder mixes the reactants to prevent separation, while the bath ensures a uniform reaction temperature. A stirrer in the cylinder provides additional mixing if needed. The rotation and stirring are gentle enough not to cause collision flocculation. The reactor chamber is completely filled with reactants; no air is present to mix with the contents and promote flocculation. A piston that constitutes an end wall of the reactor moves to accommodate the changing volume of reactants. The moving piston also drives a linear variable-differential transformer, the electrical output of which indicates the volume of the chamber and thus provides information on the stage of the polymerization reaction.

The prototype reactor holds 235 ml of fluid. Although the variation in the size of the latex particles produced in this reactor is somewhat greater than the 2% variation of particles made in space, the product should become more uniform as latex recipes are improved.

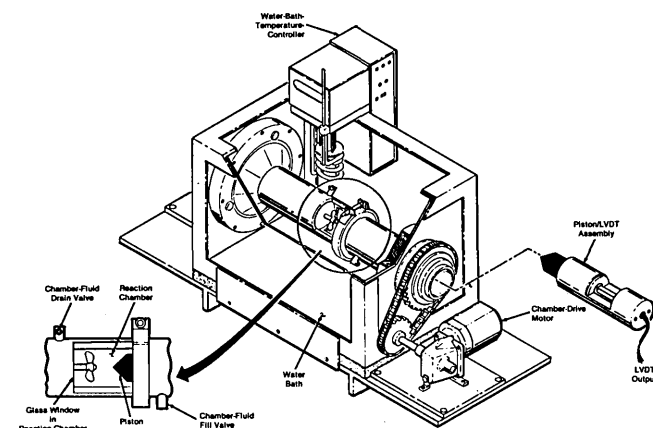


Fig. 11. Reaction chamber rotates while the polymerization of latex proceeds. A motor (not shown) at the far end of the machine turns the stirrer. The chamber is made of stainless steel with glass windows.

This work was done by Dale M. Kornfeld of Marshall Space Flight Center. Refer to MFS-28214.

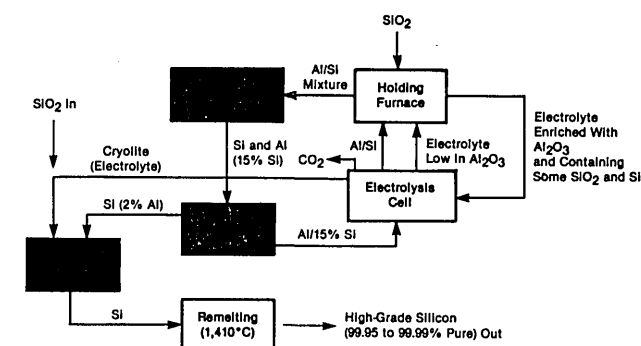


Fig. 10. Aluminum and electrolyte flow to and from an aluminum-electrolysis cell at various stages of the silicon-producing process. The electrolyte is molten cryolite.